

# SHEAR FORCE CAPACITY OF CROSS LAMINATED TIMBER BEAMS – NUMERICAL INVESTIGATIONS OF FRACTURE BEHAVIOUR

Henrik Danielsson<sup>1</sup>, Erik Serrano<sup>2</sup>

**ABSTRACT:** This paper deals with numerical investigations of cross laminated timber (CLT) beams. Previous investigations have revealed discrepancies between experimental test results and suggested design methods regarding shear force capacity of such beams. To gain further understanding of the failure behaviour and the shear force capacity, nonlinear finite element analyses have been performed, using a cohesive zone modelling approach for representation of the fracture behaviour of the bonding between laminations. Numerical results, analytical model predictions and findings from experimental tests are compared regarding the influence of different beam geometry parameters. The aim of the present work is to gain further understanding of the failure behaviour and shear force capacity of CLT beams, as such knowledge is needed for development of rationally based and reliable design methods.

**KEYWORDS:** cross laminated timber, in-plane shear, fracture mechanics, finite element modelling

## 1 – INTRODUCTION

When used as a beam element, cross laminated timber (CLT) provides advantages compared to conventional glulam thanks to the reinforcing effect of the transverse layers with respect to stresses perpendicular to the beam axis. The stress distribution in CLT beams is however complex and design verifications regarding shear force capacity are non-trivial. Increased understanding of the mechanical behaviour and failure mechanisms is needed to better exploit the use of CLT as efficient beam elements in timber construction.

## 2 – BACKGROUND

Currently available design methods for CLT beams are based on simplified analytical models regarding the internal force and stress distribution, see e.g. [1]. Regarding shear failure mechanism III (FM III), involving longitudinal and rolling shear stresses acting in the crossing areas (the areas shared between flatwise bonded laminations of adjacent layers), criteria formulated in terms of rolling shear strength and torsional shear strength have been suggested in [2,3] and are for example incorporated in the Canadian CLT Handbook [4].

These failure criteria and the models suggested for stress analysis are based on several assumptions, e.g. linear elastic material behaviour.

Modifications of the model from [2,3] for stress analysis for shear FM III have been suggested in [1]. These two models differ regarding predicted influence of various beam geometry parameters. To evaluate the models in terms of their capabilities for prediction of load-bearing capacities, tests of prismatic five-layer CLT beams were carried out [5], using the test setup shown in Fig. 1.

All beams in that study, [5], had the same gross cross section ( $t_{\text{gross}} = 140$  mm and  $h = 600$  mm) and the influence of three geometry parameters was studied:

- lamination width:  $b_x = b_y = 100$  mm and  $b_x = b_y = 150$  mm
- CLT layup: 40-20-20-20-40, 34-20-33-20-34 and 25-20-50-20-25
- the length of the beam overhang at the support:  $L_e = 120$  mm and  $L_e = 400$  mm

An overview of the beam geometries for the different test series is given in Tab. 1, with definitions of geometry parameters according to Figs. 1 and 2.

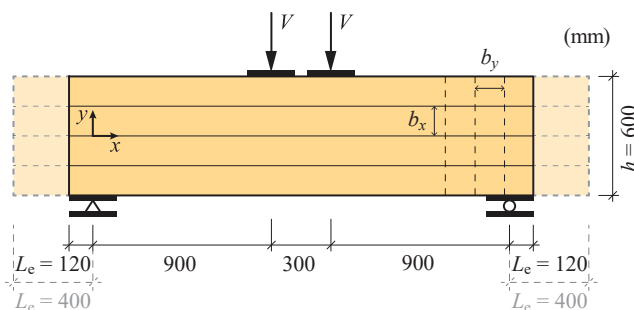


Figure 1. Experimental test setup for prismatic CLT beams (left) and an example of a CLT beam during testing (right).

<sup>1</sup> Henrik Danielsson, Division of Structural Mechanics, Lund University, Lund, Sweden, [henrik.danielsson@construction.lth.se](mailto:henrik.danielsson@construction.lth.se)

<sup>2</sup> Erik Serrano, Division of Structural Mechanics, Lund University, Lund, Sweden, [erik.serrano@construction.lth.se](mailto:erik.serrano@construction.lth.se)

The experimental results presented in [5] indicate very little or no influence of the lamination width and the CLT layup on the load-bearing capacity. In this respect, the test results contradict predictions of load-bearing capacities according to the abovementioned design methods.

The experimental study in [5] was designed to investigate the shear force capacity and a setup with a low span-to-depth ratio was hence used:  $L/h = 3.5$ . The final failures at maximum load (or after reaching maximum load) were however related to bending, with cracking and failure of the longitudinal laminations on the tension side of the beams. A gradual, and in many cases quite considerable, decrease in stiffness of the load vs deflection response was found before reaching the maximum load.

The maximum bending stress, evaluated from technical beam theory at maximum load, was relatively low with mean values between 29.2 and 31.8 MPa for the test series presented in [5]. Previous tests of five-layer CLT beams, reported in [6], with similar cross section dimensions and layups but with greater span-to-depth ratio gave considerably greater mean values of the bending stress at failure: 39.7 MPa for  $L/h = 4800/600 = 8$  and 36.5 MPa for  $L/h = 2400/600 = 4$ .

Gradual damage of the bonding between laminations over the crossing areas is a possible explanation for the gradual loss of stiffness during loading. Such damage leads to decreasing composite action, stress redistribution and increasing bending of the individual longitudinal laminations. At increasing loading, bending failure may occur before complete shear failure occurs. This suggests that shear stresses acting over the crossing areas may be of great importance for the load-bearing capacity, although the final failure is not labelled as shear failure.

The main aim of the present study is to gain knowledge and contribute to further understanding of the failure mechanisms for CLT under in-plane beam loading. A numerical study of the CLT beam tests reported in [5], with a test setup according to Fig. 1 and beam geometry parameters according to Tab. 1, has been performed. The approach adopted includes modelling the gradual damage of the bonding over the crossing areas, which enables studies of the influence of this mechanism on the internal force distribution and on the global beam response.

Table 1: Test series geometries, with dimensions in mm.

	$t_{x,1}$	$t_{y,1}$	$t_{x,2}$	$t_{y,2}$	$t_{x,3}$	$b_x = b_y$	$L_e$
A-100-L	40	20	40	20	40	100	400
A-100-S	40	20	40	20	40	100	120
A-150-L	40	20	40	20	40	150	400
A-150-S	40	20	40	20	40	150	120
B-100-L	33	20	34	20	33	100	400
B-100-S	33	20	34	20	33	100	120
B-150-L	33	20	34	20	33	150	400
B-150-S	33	20	34	20	33	150	120
C-100-L	25	20	50	20	25	100	400
C-100-S	25	20	50	20	25	100	120
C-150-L	25	20	50	20	25	150	400
C-150-S	25	20	50	20	25	150	120

### 3 – ANALYTICAL MODELS

The analytical model for stress analysis of CLT beams presented in [1] originates from the work of Flaig & Blass, see [2] and [3]. To enable comparisons to the numerical results of the present study, some expressions for stresses and forces for relevant failure modes are given below.

The considered analytical models are based on assumptions of linear elastic material behaviour and kinematic assumptions according to technical beam theory; plane beam cross sections remain plane during bending deformation. Beam geometry parameters according to Fig. 2 are considered and notations for lamination forces and moments are given in Fig. 3.

The normal stress parallel to grain in the longitudinal layers, due to a bending moment  $M$ , can be expressed as

$$\sigma_x = -\frac{M}{I_{\text{net}}}y \quad (1)$$

where the net moment of inertia is given by  $I_{\text{net}} = t_x h^3/12$  and where  $t_x = \sum t_{x,k}$ .

The normal stress in a specific lamination  $i,k$  can also be expressed by the lamination normal force  $N_{i,k}$  and the lamination bending moment  $M_{i,k}$ , according to

$$\sigma_{x,i,k} = \frac{N_{i,k}}{A_{i,k}} - \frac{M_{i,k}}{I_{i,k}}y_i \quad (2)$$

where  $A_{i,k} = t_{x,k}b_x$ ,  $I_{i,k} = t_{x,k}b_x^3/12$  and where  $y_i$  is a local coordinate with  $y_i = 0$  at the centre of the lamination.

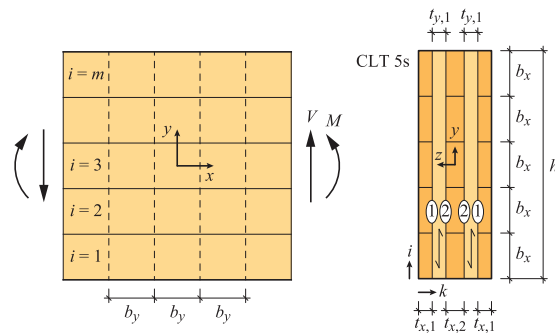


Figure 2. Definition of beam geometry parameters, adapted from [1].

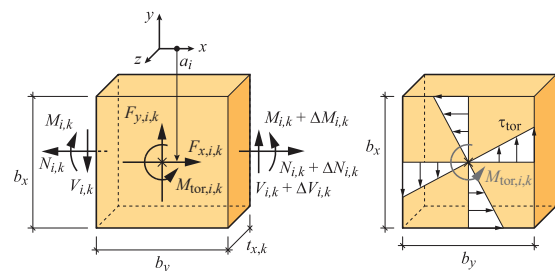


Figure 3. Forces and moments acting on a segment of a longitudinal lamination (left) and assumed shear stress distribution over a crossing area due to the torsional moment  $M_{\text{tor}}$  (right), adapted from [1].

The torsional moments  $M_{\text{tor},i,k}$  in crossing areas for CLT with five layers can according to [7] can be expressed as

$$M_{\text{tor},i,k} = \frac{V b_y t_{x,k}}{n_{\text{CA},k} t_x} \left( \alpha_i - \frac{1}{m^3} \right) \quad (3)$$

where  $m$  is the total number of longitudinal laminations in the beam depth direction and where  $n_{\text{CA},k}$  is the number of crossing areas that the considered longitudinal lamination shares with adjacent and transverse laminations, i.e.  $n_{\text{CA},1} = 1$  and  $n_{\text{CA},2} = 2$ . The parameter  $\alpha_i$  describes the distribution of the lamination shear forces  $V_{i,k}$  in the beam depth direction, according to a parabolic shape with maximum values of  $\alpha_i$  and  $V_{i,k}$  close to the beam centreline.

The torsional moments cause torsional shear stresses in the crossing areas (rolling shear and longitudinal shear), which are the dominating stresses for shear FM III, see [1]. According to (3), the shear force capacity with respect to FM III should be governed by the element layup and the maximum value of the ratio  $(1/n_{\text{CA},k}) \cdot (t_{x,k}/t_x)$ .

In the original model suggested by Flaig & Blass [2,3], the values of the torsional moments are based on (implicitly) assuming a uniform distribution in the beam width direction, irrespective of the element layup. This corresponds to assuming  $(1/n_{\text{CA},k}) \cdot (t_{x,k}/t_x) = 0.25$  in (3), for CLT with five layers. The design equation suggested in [2,3] does further not consider a non-uniform distribution of torsional moments in the beam depth direction. This corresponds to assuming the parameter  $\alpha_i = 1/m$  in (3). The expression for the torsional moments, corresponding to (3), can with these assumptions be expressed as

$$M_{\text{tor},i,k} = \frac{V b_y}{n_{\text{CA}}} \left( \frac{1}{m} - \frac{1}{m^3} \right) \quad (4)$$

where  $n_{\text{CA}}$  is the total number of crossing areas in the beam width direction, i.e.  $n_{\text{CA}} = 4$  for five-layer CLT.

The difference between (3) and (4) was one of the motivations for using the layouts A, B and C according to Tab. 1 for the tests of CLT beams reported in [5]. The (maximum) values of the abovementioned ratio  $(1/n_{\text{CA},k}) \cdot (t_{x,k}/t_x)$  are for these three layouts 0.40, 0.33 and 0.25, respectively.

The non-uniform distribution of the torsional moments in the beam width direction, according to (3), yields a predicted shear force capacity for FM III which is considerably greater for layout C compared to layout A. Predictions of shear force capacity for FM III according to (4) are equal for all layouts (A, B and C), since the influence of the individual layer widths  $t_{x,k}$  is not taken into account.

#### 4 – FINITE ELEMENT MODELLING

CLT beams with geometries and loading conditions according to Tab. 1 and Fig. 1 have been studied, using nonlinear finite element (FE) models and a cohesive zone modelling approach implemented in the software Abaqus [8].

The individual timber laminations were modelled as separate 3D linear elastic solids with orthotropic stiffness properties according to Tab. 2. Rectilinear material principal directions were assumed with the longitudinal (L) direction along the length of the laminations and the tangential (T) and radial (R) directions along the lamination width and thickness directions, respectively. The laminations were modelled using linear 8-node elements with full integration (denoted C3D8 in Abaqus). Results presented in Section 5 are based on FE-meshes consisting of approximately cubically shaped elements with a side length of about 8 mm. Symmetry in two planes was considered for all models.

The steel plates at the load introduction and at the supports were modelled using rigid surfaces. Contact was modelled between the rigid surfaces and the transverse laminations. This contact was modelled as hard contact with friction, with a coefficient of friction  $\mu = 0.2$ . The loading was applied as prescribed displacement.

The bonding between the laminations of adjacent layers was modelled using a surface-to-surface contact formulation, with hard contact in compression and with cohesive behaviour and strain-softening for the two in-plane shear directions and tension. This formulation is defined by the material strengths in the two in-plane shear directions ( $f_{s1}$  and  $f_{s2}$ ) and the tensile strength ( $f_n$ ), the corresponding initial stiffnesses ( $k_{s1}$ ,  $k_{s2}$  and  $k_n$ ), the fracture energy ( $G_f$ ) and a softening law.

The initiation of softening was defined by a maximum stress criterion according to

$$\max \left\{ \frac{\langle \sigma_n \rangle}{f_n}, \frac{\tau_{s1}}{f_{s1}}, \frac{\tau_{s2}}{f_{s2}} \right\} = 1.0 \quad (5)$$

where  $\tau_{s1}$  and  $\tau_{s2}$  are the two in-plane shear components and where  $\sigma_n$  refers to the normal (tensile) stress over the crossing area. Linear softening was assumed.

This modelling approach has previously been used in [9] and [10] for studies of test setups, composed of two orthogonal laminations and a single crossing area, and designed for determination of rolling shear and torsional shear strength properties. Similar (or identical) values of model parameters used in those studies were used also for the present analyses:  $f_{s1} = f_{s2} = 3.0$  MPa,  $f_n = 5.0$  MPa,  $k_{s1} = k_{s2} = k_n = 300$  N/mm<sup>3</sup> and  $G_f = 1.2$  Nmm/mm<sup>2</sup>.

Table 2: Material stiffness parameters for timber laminations.

Modulus of Elasticity	$E_L$	12 000	MPa
	$E_T$	400	MPa
	$E_R$	600	MPa
Shear modulus	$G_{LT}$	750	MPa
	$G_{LR}$	600	MPa
	$G_{TR}$	75	MPa
Poisson's ratio	$\nu_{LT}$	0.50	-
	$\nu_{LR}$	0.50	-
	$\nu_{TR}$	0.33	-

For analyses presented in [9] and [10], reasonable agreement was found between numerical predictions of load-bearing capacity of single crossing areas and tests.

By modelling strain softening after reaching the local material strength, the formation and development of fracture process zones in the crossing areas can be simulated. Since the timber laminations are modelled as linear elastic, failure and cracking due to for example tension parallel to grain is however not accounted for.

#### 4.1 INFLUENCE OF FE-MESH SIZE

A study of the influence of the (finite) element size on the response was carried out for a beam geometry according to test series C-150-S, see Tab. 1. Results for the maximum shear force  $V_{\max}$  and the initial (elastic) beam stiffness  $\Delta V/\Delta v$  are shown in Fig. 4. The results are normalized to the results for the reference element size of about 8 mm, which was used for analyses presented in Section 5. See Fig. 8 for the response in terms of shear force  $V$  vs displacement  $v$  for the reference case.

#### 4.2 INFLUENCE OF CONTACT STIFFNESS

A study of the influence of the initial stiffness of the contact area  $k_{\text{init}}$  ( $= k_{s1} = k_{s2} = k_n$ ) on the response was also carried out for a beam geometry according to test series C-150-S, see Tab. 1. Results for the maximum shear force  $V_{\max}$  and the initial (elastic) beam stiffness  $\Delta V/\Delta v$  are shown in Figs. 5 and 6, respectively. The results are normalized to the results for the reference stiffness value  $k_{\text{init}} = 300 \text{ N/mm}^3$ , which was used for analyses presented in Section 5. See Fig. 8 for the response in terms of shear force  $V$  vs displacement  $v$  for the reference case.

Increasing the initial stiffness to values above  $900 \text{ N/mm}^3$  resulted in numerical issues and convergence problems before reaching the maximum load. Results presented in Fig. 5 are hence given only for  $k_{\text{init}} \leq 900 \text{ N/mm}^3$ . The maximum load is however influenced only to a very limited extend by the contact area stiffness. The initial beam stiffness  $\Delta V/\Delta v$  is clearly influenced for low values of the contact area stiffness but it is not influenced very much for stiffness values  $k_{\text{init}} \geq 300 \text{ N/mm}^3$ .

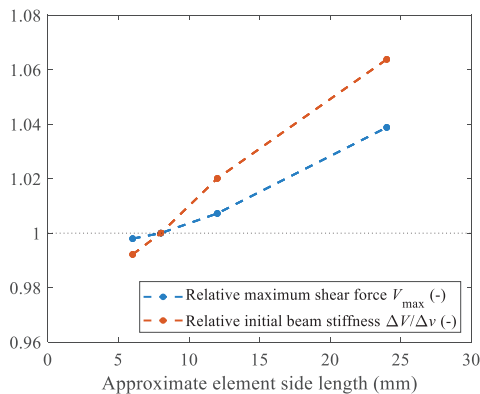


Figure 4. Relative maximum shear force  $V_{\max}$  and relative initial beam stiffness vs element size, normalized with respect to element size 8 mm.

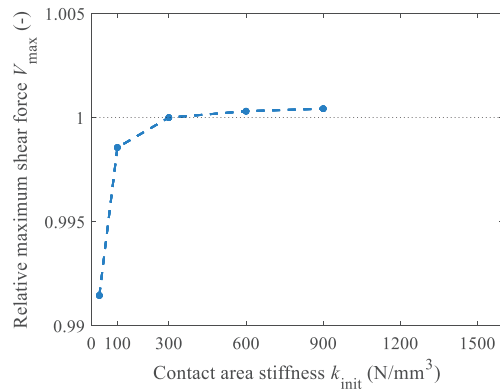


Figure 5. Relative maximum shear force  $V_{\max}$  vs contact area stiffness, normalized with respect to  $k_{\text{init}} = 300 \text{ N/mm}^3$ .

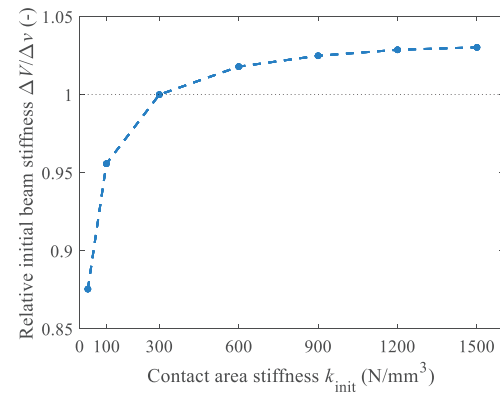


Figure 6. Relative initial beam stiffness  $\Delta V/\Delta v$  vs contact area stiffness, normalized with respect to  $k_{\text{init}} = 300 \text{ N/mm}^3$ .

The distribution over the beam depth of the normal stress  $\sigma_x$  in the longitudinal laminations is shown in Fig. 7, for different values of the stiffness  $k_{\text{init}}$ . These results are based on (2) and on lamination normal forces  $N_{i,k}$  and bending moments  $M_{i,k}$  as found from linear elastic FE-analyses by integration of stresses over the cross sections of the longitudinal laminations at the beam midspan (the plane of symmetry in  $x$ -direction). The stress values are normalised with respect to the maximum normal stress according to the analytical model, according to (1).

The results of the numerical models show staggered stress distributions with more bending of the individual laminations, compared to the assumption of the analytical model with a linear stress distribution over the entire beam depth. There are very small differences in the numerical results between the internal and external longitudinal layers (in the beam width direction), less than 0.2%.

The mean values (for the two layers in the beam width direction) of the maximum normalised stress are 1.309, 1.222, 1.205 and 1.202 for initial stiffness values  $k_{\text{init}}$  of 30, 300, 900 and  $1500 \text{ N/mm}^3$ , respectively. The normal stress distribution thus seems to be insensitive to the assumed initial stiffness for values above  $300 \text{ N/mm}^3$ .

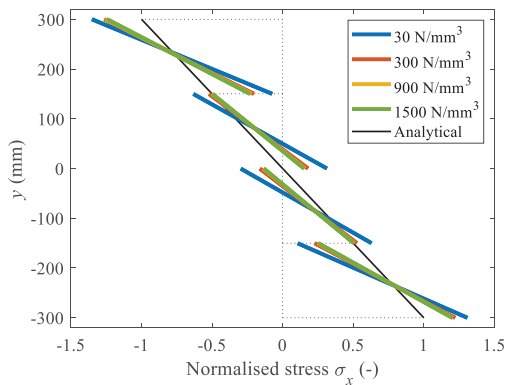


Figure 7. Normalised stress over beam depth for FE-analyses at linear elastic stage, for different values of the contact area stiffness  $k_{init}$ .

The staggered normal stress distribution and the differences compared to the linear stress distribution according to technical beam theory, (1), is partly related to the specific geometry, with a low span-to-depth ratio and load introduction close to midspan (where the stresses are evaluated). Increasing the distance between the point loads from 300 mm to 600 mm (see Fig. 1) gives a mean value of the maximum normalised stress of about 1.11 for an initial stiffness value  $k_{init} = 300 \text{ N/mm}^3$ .

## 5 – RESULTS AND DISCUSSION

Numerical results in terms of the shear force  $V$  vs beam deflection  $v$  for a beam geometry according to test series C-150-S are shown in Fig. 8. Four load levels are marked with circles:  $V_0$  represents the last load step before fracture initiation in the crossing areas,  $V_{40}$  represents the load at which the maximum normal tensile stress  $\sigma_x = 40 \text{ MPa}$ ,  $V_{max}$  represents the maximum shear force and  $V_{end}$  represents the load level at the end of the analysis.

Normal stress distributions over the beam depth at midspan are shown in Fig. 9 for the four load levels given in Fig. 8, with both normalised and absolute values. These stress distributions were determined in the same manner as described above, i.e. from (2) and from lamination normal forces  $N_{i,k}$  and lamination bending moments  $M_{i,k}$  as found from the FE-analyses by integration of stresses over the cross sections of the longitudinal laminations at beam midspan.

From the FE-analysis, a maximum normal tensile stress  $\sigma_x = 40 \text{ MPa}$  was found at a shear force of  $V_{40} = 207 \text{ kN}$ . The maximum normal tensile stress at this level of external load is only 30.9 MPa according to the analytical model and (1).

Results presented in Fig. 9 further show how the bending of the individual laminations gradually increases as the prescribed displacement is increased, especially for the two centrally placed laminations.

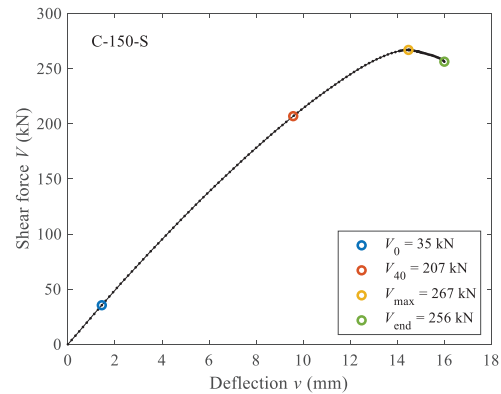


Figure 8. Shear force  $V$  vs beam deflection  $v$  for C-150-S.

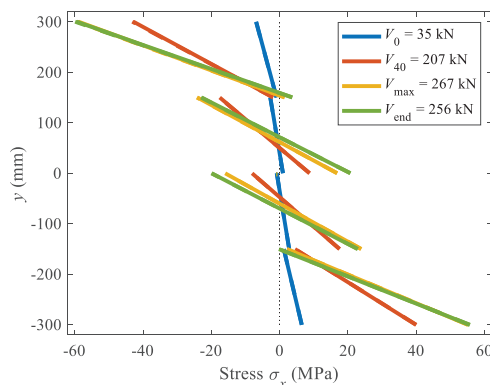
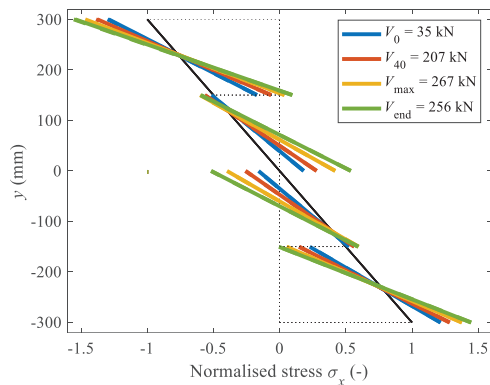


Figure 9. Stress over beam depth for FE-analyses at different stages of the shear force vs beam deflection response for C-150-S.

Comparisons between the response in terms of shear force  $V$  vs beam deflection  $v$  as found from experimental tests and as found from FE-analyses are presented in Fig. 10, for all test series given in Tab. 1. The marks (circles) for the numerical results indicate the respective load levels at which the maximum parallel to grain tensile stress in the longitudinal laminations at beam midspan corresponds to  $\sigma_x = 40 \text{ MPa}$ .

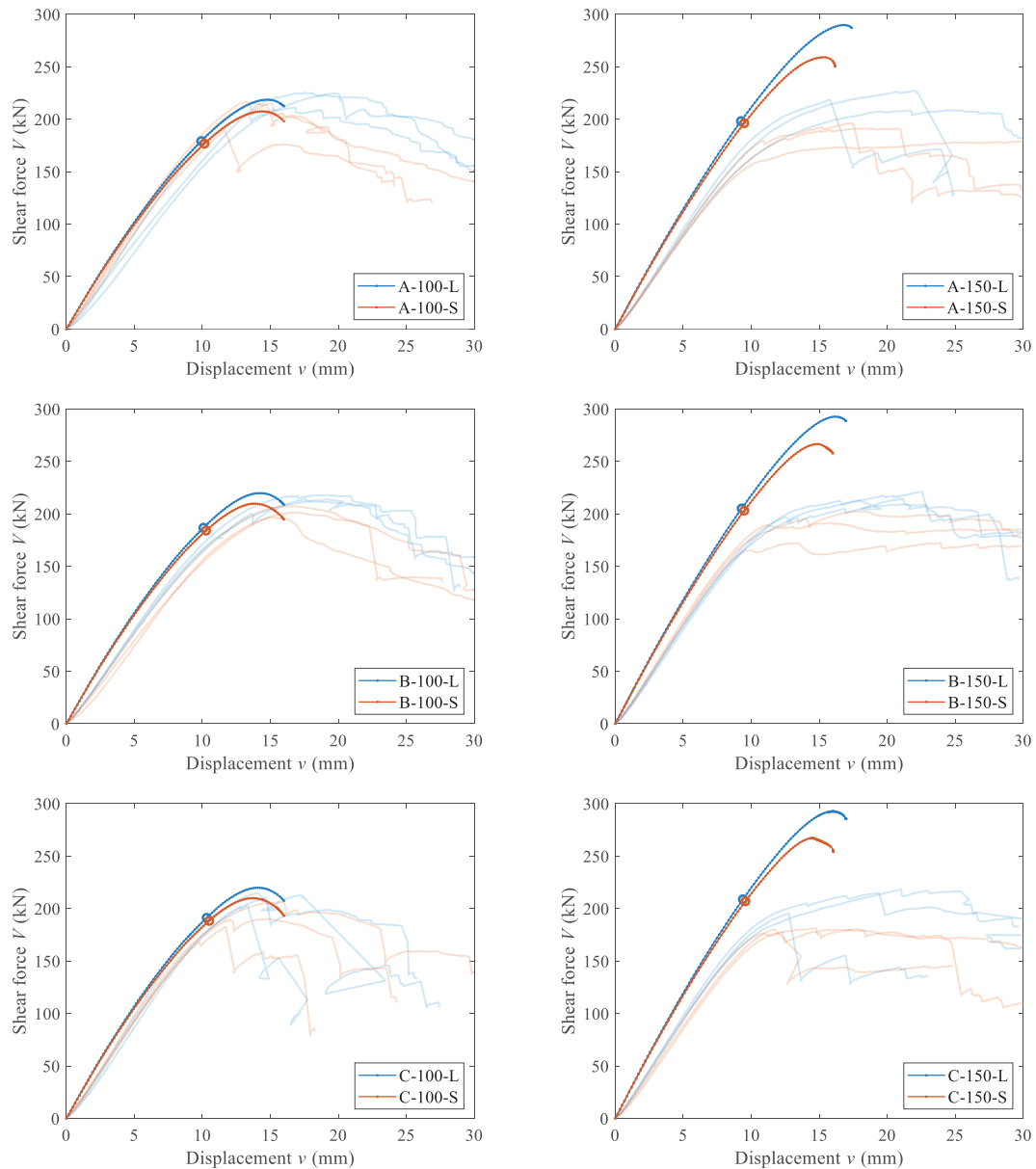


Figure 10. Experimental and numerical results in terms of shear force  $V$  vs beam deflection  $v$  for all test series reported in [5]. The circles represent the load level denoted  $V_{40}$ , which corresponds to a maximum parallel to grain tensile stress  $\sigma_x = 40$  MPa, see Figs. 8 and 9.

The beam geometries for the test series shown in Fig. 10 differ regarding three aspects (see Tab. 1): the element layup (A, B and C), the lamination width  $b$  (100 mm and 150 mm) and the length of the overhang at the support  $L_e$  (120 mm (S) and 400 mm (L)).

For all test series, the mean value of the experimentally obtained maximum shear force was greater for test series with a long overhang at the support (L,  $L_e = 400$  mm) than for test series with a short overhang at the support (S,  $L_e = 120$  mm). This trend was also found from the FE-analyses, with greater values of  $V_{\max}$  for the test series with a long overhang at the support.

It is however important to stress that the FE-models are based on linear elastic material behaviour for the laminations and that fracture and softening is only modelled within the bonding areas between laminations. The FE-models can hence not be expected to accurately capture the behaviour of the tests at load levels around the maximum load, since cracking and failure of the longitudinal laminations due to bending was observed in the tests. The range of values for the experimentally obtained maximum shear forces, 180–220 kN, agrees well with the range of shear forces corresponding to a maximum tensile stress  $\sigma_x = 40$  MPa; 177–209 kN.

## 5.1 FRACTURE IN CROSSING AREAS

The development of fracture process zones over the crossing areas is illustrated in Fig. 11, where the internal longitudinal laminations ( $k=2$ ) are shown at four different load levels, for beam geometry C-150-S (see also Figs. 8 and 9). Softening is first initiated in the crossing areas at the beam centreline, connecting the longitudinal laminations to the fourth transverse lamination from the left. As loading is increased, softening is also initiated in several crossing areas in the beam length direction and at the upper- and lowermost crossing areas, see Fig. 11a).

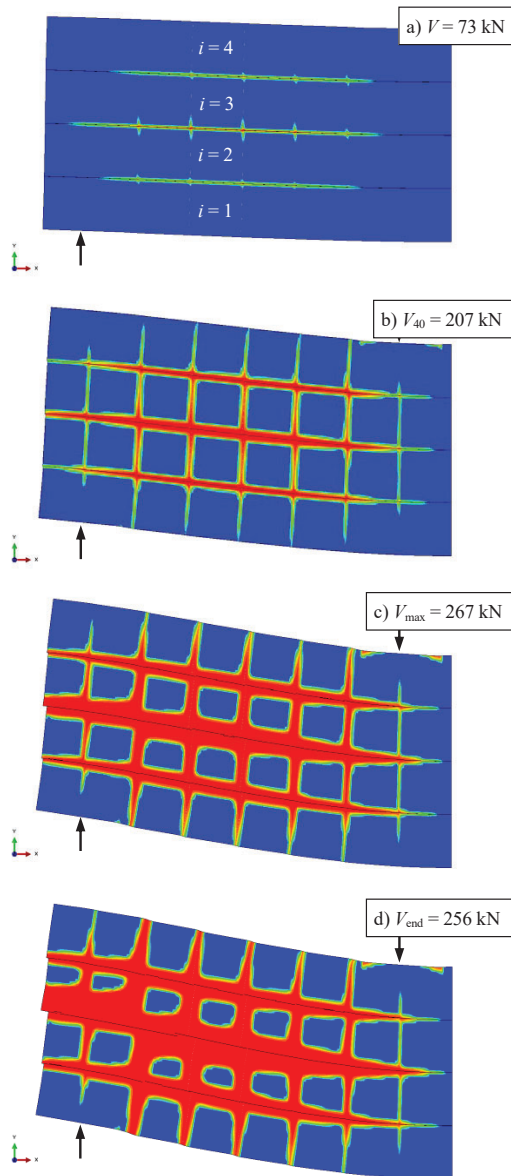


Figure 11. Development of fracture process zones over the crossing areas on the internal longitudinal laminations for C-150-S, by Abaqus damage parameter (CSDMG). Deep blue represents undamaged state (linear elastic) and deep red represents severely damaged state. Deformations are scaled by a factor of 10.

The zones experiencing softening and diminishing stress transferring capacity expand during further loading. At a shear force of  $V_{40} = 207$  kN, see Fig. 11b), fracture process zones are found along all four sides of the perimeter of the crossing areas which are centrally placed in the beam depth direction ( $i = 2, 3$ ) and located between the loading point and the support point.

When reaching the maximum load of  $V_{\max} = 267$  kN, see Fig. 11c), the damaged zones cover a large part of several crossing areas. At this stage, significant horizontal sliding between the two centrally placed longitudinal laminations can also be seen. During loading by increased prescribed displacement  $v$ , and decreasing shear force  $V$ , the fracture process zones extend further and the sliding between the neighbouring longitudinal laminations increases, see Fig. 11d).

Results for crossing area torsional moments  $M_{\text{tor},i,k}$  vs beam deflection  $v$  are shown in Figs. 12 and 13, for beam geometries C-150-S and A-150-S. The torsional moments were determined from integration of shear stresses in the crossing areas for a location in the beam length direction corresponding to the fourth transverse lamination from the left side of the beam as seen in Fig. 11.

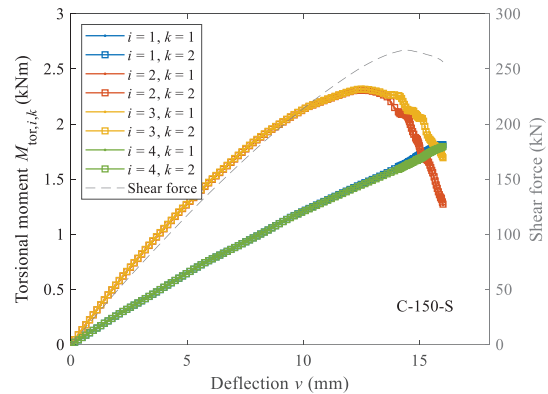


Figure 12. Crossing area torsional moments  $M_{\text{tor},i,k}$  (and shear force  $V$ ) vs the beam deflection  $v$  for beam geometry C-150-S.

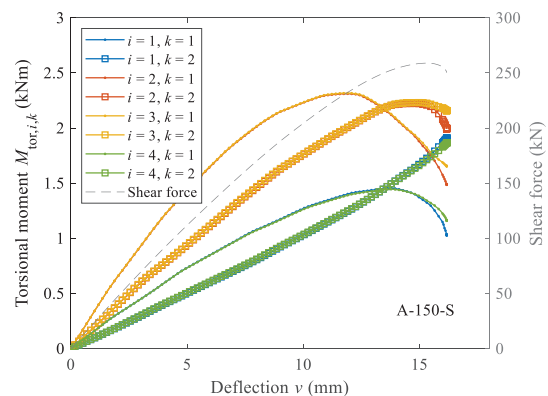


Figure 13. Crossing area torsional moments  $M_{\text{tor},i,k}$  (and shear force  $V$ ) vs the beam deflection  $v$  for beam geometry A-150-S.

Beam geometry C-150-S, with layup 25-20-50-20-25, has a constant value of the ratio  $(1/n_{CA,k}) \cdot (t_{x,k}/t_x) = 0.25$  for all crossing areas ( $k = 1$  and  $2$ ) in the beam width direction. The analytical model, according to (3), hence yields equal values of the torsional moments for crossing areas  $k = 1$  and  $2$  for a certain lamination placement  $i$  in the beam depth direction, i.e.  $M_{tor,i,1} = M_{tor,i,2}$ . This characteristic is indeed confirmed by the FE-analysis. As can be seen in Fig. 12 for C-150-S,  $M_{tor,i,k}$  are almost identical for the two crossing areas in the beam width direction ( $k = 1$  and  $2$ ). Differences between the two crossing areas in the width direction are seen only at late stages of loading.

Furthermore, (3) gives different values of the torsional moments  $M_{tor,i,k}$  in the beam depth direction, due to the factor  $\alpha_i$ . For the considered geometry, C-150-S, with  $m = 4$  laminations in the beam depth direction, the values of the factor  $\alpha_i$  are  $\alpha_1 = \alpha_4 = 5/32$  and  $\alpha_2 = \alpha_3 = 11/32$  according to [8]. Equation (3) then predicts a ratio between the torsional moments in the centrally placed crossing areas ( $i = 2$  and  $3$ ) and externally placed crossing areas ( $i = 1$  and  $4$ ) of 2.33. This agrees rather well with the numerical results during the initial (elastic) stage of loading, before initiation of softening. The ratios between the corresponding torsional moments found from the FE-analysis and shown in Fig. 12 are in the range of 2.0–2.1 during this stage.

However, as softening is initiated in the crossing areas, stress redistribution takes place and the relative distribution of the torsional moments in the beam depth directions changes. The torsional moments in the centrally placed crossing areas ( $i = 2$  and  $3$ ) reach their respective maximum values at a shear force of about 250 kN, see Fig. 12. During further loading, with increased prescribed displacement  $v$  (and eventually decreasing shear force), a state is reached with almost equal torsional moments for all crossing areas, both in the beam width and in the beam depth direction.

Beam geometry A-150-S, with layup 40-20-20-20-40, has ratios  $(1/n_{CA,k}) \cdot (t_{x,k}/t_x) = 0.40$  for  $k = 1$  and  $0.10$  for  $k = 2$ . The analytical model, according to (3), hence yields different values of the torsional moments  $M_{tor,i,k}$  for crossing areas  $k = 1$  and  $2$  for a certain lamination  $i$ . The ratio between the torsional moments of the external ( $k = 1$ ) and the internal crossing area ( $k = 2$ ) in the beam width direction is hence 4.0, according to (3). The non-uniform distribution, in the width direction, of the torsional moments, is indeed confirmed by the FE-analysis. However, as evidenced by the results seen in Fig. 13, the ratios between the torsional moments for  $k = 1$  and  $k = 2$  are smaller, approximately 1.7 during the initial (elastic) stage.

As loading is increased and fracture process zones develop, the distribution of the torsional moments between the crossing areas changes. Before reaching the maximum shear force for A-150-S, the torsional moments are greater in the internal crossing areas ( $k = 2$ ) than in the external crossing areas ( $k = 1$ ). As seen in Fig. 13, this changes during the course of loading. When the load

approaches its maximum, from approximately 13.5 mm deflection, instead the torsional moments for  $k = 2$  are greater than for  $k = 1$ .

## 5.2 LONGITUDINAL LAMINATIONS

The beam gross cross section is exposed to bending (and shear) while the individual longitudinal laminations are exposed to a combination of bending and axial compression/tension (and shear). The gradual damage, which leads to a loss of stiffness of the connections between longitudinal and transverse laminations, influences the bending behaviour of the gross cross section and the individual laminations. As softening is initiated in the crossing areas, the contact stiffness decreases, and the individual longitudinal laminations are exposed to more bending in relation to axial compression/tension.

The lamination bending moments  $M_{i,k}$  and normal forces  $N_{i,k}$  for beam geometries C-150-S and A-150-S are shown in Figs. 14 and 15, respectively. The values are determined by integration of stresses over the lamination cross sections at the beam midspan (at the plane of symmetry in the  $x$ -direction). For laminations in the plane of symmetry in the  $z$ -direction ( $k = 2$ ), values of  $N_{i,2}$  and  $M_{i,2}$  refer to the full cross section of the laminations, i.e.  $A_{i,2} = b_x t_{x,2}$ .

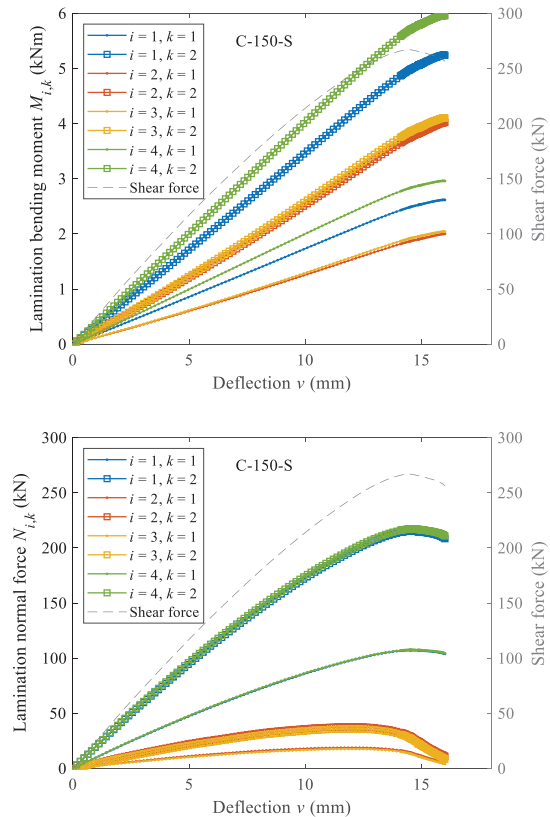


Figure 14. Lamination bending moments  $M_{i,k}$  (top) and normal forces  $N_{i,k}$  (bottom) vs the beam deflection  $v$  for beam geometry C-150-S.

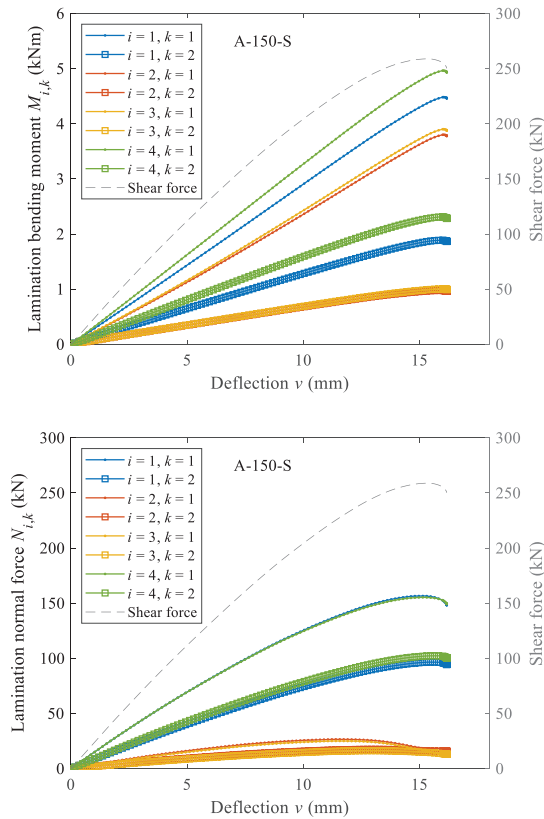


Figure 15. Lamination bending moments  $M_{i,k}$  (top) and normal forces  $N_{i,k}$  (bottom) vs the beam deflection  $v$  for beam geometry A-150-S.

As can be seen in Figs. 14 and 15, the lamination bending moments  $M_{i,k}$  continuously increase for all laminations  $i,k$  for both beam geometries, at least up to the point where the respective maximum shear forces  $V_{\max}$  are reached. For beam geometry C-150-S, the bending moments  $M_{i,k}$  also keep increasing after reaching the maximum load. The lamination normal forces  $N_{i,k}$  do however reach their respective maximum values before the respective maximum shear forces are reached.

For beam geometry C-150-S, see Fig. 14, the maximum normal forces in the centrally placed laminations,  $i = 2$  and 3 (i.e.  $N_{2,1}$ ,  $N_{2,2}$ ,  $N_{3,1}$  and  $N_{3,2}$ ), reach their respective maximum values at a beam displacement  $v \approx 12$  mm and a shear force  $V \approx 245$  kN. At further increased loading by prescribed displacement, the gradual damage and softening over the crossing areas (see Fig. 11) result in increased bending of the individual laminations and the ratios between the respective lamination bending moments  $M_{i,k}$  and normal forces  $N_{i,k}$  increase.

The same general observations are also valid for beam geometry A-150-S, see Fig. 15. For this geometry, the increased bending of individual laminations is most obvious for laminations  $i = 2, 3$  and  $k = 1$ , i.e. the centrally placed laminations in the beam depth direction and the external layer in the beam width direction.

For beam geometry A-150-S, the initiation of fracture in the crossing areas takes place in the corresponding location, i.e.  $i = 2, 3$  and  $k = 1$ . As can be seen in Fig. 13, the torsional moments  $M_{\text{tor},2,1}$  and  $M_{\text{tor},3,1}$  are initially the greatest but diminish considerably after reaching their respective maximum values at a beam displacement  $v \approx 12$  mm and a shear force  $V \approx 235$  kN.

### 5.3 LENGTH OF BEAM OVERHANG

Some final observations can be made regarding the influence of the length of the beam overhang at the support,  $L_e$ , see Fig. 1. From tests reported in [5], the mean values of the maximum shear forces were found to be slightly greater (about 10%) for the test series with a long overhang at the support ( $L, L_e = 400$  mm) compared to the test series with a short overhang (S,  $L_e = 120$  mm). From the numerical results presented in Fig. 10, the maximum shear forces are also consistently greater for the test series with a long overhang at the support. There are however only small differences between the different overhang lengths regarding the shear force level  $V_{40}$ , corresponding to a maximum normal tensile stress  $\sigma_x = 40$  MPa.

The distributions of parallel to grain normal stress in the longitudinal laminations, as found from the FE-analyses, are very similar for geometries C-150-L ( $L_e = 400$  mm) and C-150-S ( $L_e = 120$  mm) in the initial stage of loading, roughly up to a maximum tensile stress of 35–40 MPa. At further loading, the loss of stiffness over the crossing areas results in considerable sliding between the longitudinal laminations for C-150-S. For C-150-L, the crossing areas in the overhang zone are not severely damaged and the overhang partly prevents sliding between the longitudinal laminations. Illustrations of deformations and normal stresses are shown in Fig. 16, for the two respective final stages of loading according to Fig. 10.

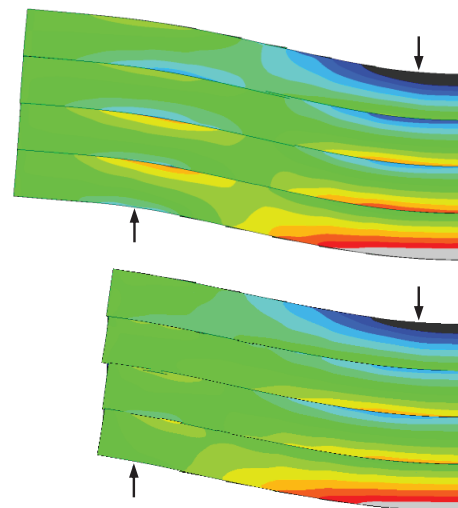


Figure 16. Parallel to grain normal stress at final stage of analyses for beam geometries C-150-L (top) and C-150-S (bottom). Dark grey represents stresses  $\sigma_x \leq -45$  MPa and light grey represents stresses  $\sigma_x \geq 45$  MPa. Deformations are scaled by a factor of 10.

## 6 – CONCLUDING REMARKS

The analytical model for the torsional moments  $M_{\text{tor},i,k}$  according to (3) appears to capture the distribution of torsional moments with reasonable accuracy in the elastic range, compared to results of FE-analyses presented in this paper. This has also been shown in previous numerical studies based on linear elastic material behaviour, see e.g. [1,11].

With the approach adopted in the present paper, allowing for gradual damage and softening in the crossing areas, it has however been shown that the distributions of torsional moments between crossing areas in the beam width and depth directions change during loading. The initial elastic stress distribution may hence not be directly relevant for prediction of the ultimate load-bearing capacity. Other distributions with a (more or less) uniform distribution of torsional moments may be more relevant, for example as suggested in (4), see [2,3]. Considering approaches for practical design of CLT beams, it may be reasonable to disregard the influence of the element layup in terms of the individual layer thicknesses.

Test results from [5] and numerical results presented here both suggest that interaction of failure mechanisms eventually lead to final failure. The only failure mechanism explicitly modelled in the current FE-analyses is failure in the crossing areas, while linear elastic material behaviour is assumed for the timber laminations. The maximum tensile stress parallel to the grain in the longitudinal laminations (at maximum load) is in the range of 47–53 MPa for test series with lamination width  $b = 100$  mm and in the range of 55–64 MPa for test series with lamination width  $b = 150$  mm. The numerical results hence indicate that bending failure can be expected before reaching the maximum load found from the FE-analyses.

The presented numerical results suggest that the gradual damage and the softening in the crossing areas lead to increased bending of the individual longitudinal laminations and decreased composite action. This is especially seen for the longitudinal laminations which are centrally placed with respect to the beam depth direction. The applied load configuration, with a low span-to-depth ratio and with load introduction close to beam midspan, gives however a normal stress distribution which deviates from the linear stress distribution assumed according to (1) already in the initial elastic stage.

The results presented here represent ongoing work and further investigations are planned. One aspect which has currently not been thoroughly examined is the influence of the lamination width. The present analyses are further based on several assumptions regarding criteria for fracture initiation and values for material strengths, stiffnesses and fracture energy. The modelling approach used in the present work is however believed to be very useful for gaining further knowledge about the mechanical behaviour of CLT beams and is hence expected to be valuable for further development of rational and reliable methods for practical design.

## 7 – ACKNOWLEDGEMENTS

The financial support from FORMAS for the project *Strength and fracture analysis of laminated wood-based structural elements* (grant 2023-01161) is gratefully acknowledged. The computations were enabled by resources provided by *Lunarc* – the centre for scientific and technical computing at Lund University.

## 8 – REFERENCES

- [1] H. Danielsson, and M. Jeleč. A unified design proposal for shear stress prediction in crossing areas for cross laminated timber at in-plane shear and beam loading conditions. *Construction and Building Materials* 2022;355:129167.
- [2] M. Flaig. Biegeträger aus Brettsperholz bei Beanspruchung in Plattebene. PhD thesis, Karlsruhe Institute of Technology, 2013.
- [3] M. Flaig, and H.J. Blass. Shear strength and shear stiffness of CLT-beams loaded in plane. In: *Proc. CIB-W18, Paper 46-12-3*, Vancouver, Canada, 2013.
- [4] E. Karacabeyli, and S. Gagnon. *Canadian CLT Handbook 2019 Edition*. Special Publication SP-532E, FPInnovations, 2019.
- [5] H. Danielsson, T. Pazlar, E. Serrano, and B. Azinović. Experimental investigation of the shear force capacity of prismatic cross laminated timber beams. *Engineering Structures* 2024;308:117889.
- [6] H. Danielsson, E. Serrano, M. Jeleč, V. Rajčić. In-plane loaded CLT beams – Tests and analysis of element lay-up. In: *Proc. INTER, Paper 50-12-02*, Kyoto, Japan, 2017.
- [7] H. Danielsson, and E. Serrano. Cross laminated timber at in-plane beam loading – Prediction of shear stresses in crossing areas. *Engineering Structures* 2018;173:921–927.
- [8] Dassault Systemes Simulia Corp. *ABAQUS/CAE, Version 2023*, 2022.
- [9] H. Danielsson, and E. Serrano. Cross laminated timber at in-plane shear loading – Strength and fracture analysis of shear mode III. In: *Proc. WCTE, Santiago, Chile, 2021*.
- [10] H. Danielsson, and E. Serrano. Shear failure mechanism III in cross laminated timber – Numerical investigations of fracture behaviour. In: *Proc. WCTE, Oslo, Norway, 2023*.
- [11] H. Danielsson, M. Jeleč, E. Serrano, V. Rajčić. Cross laminated timber at in-plane beam loading – Comparison of model predictions and FE-analyses. *Engineering Structures* 2019;179:246–254.